MSDE

PAPER

View Article Online
View Journal | View Issue

Cite this: *Mol. Syst. Des. Eng.*, 2020, 5, 666

Effect of polymer–nanoparticle interactions on solvent-driven infiltration of polymer (SIP) into nanoparticle packings: a molecular dynamics study†

R. Bharath Venkatesh, Tianren Zhang, Neha Manohar, Kathleen J. Stebe,* Robert A. Riggleman* and Daeyeon Lee*

Received 22nd October 2019,
Accepted 20th December 2019

DOI: 10.1039/c9me00148d

rsc.li/molecular-engineering

Naturally occurring nanocomposites like nacre owe their exceptional mechanical properties to high loadings of platelets that are bridged by small volume fractions of polymers. Polymer infiltration into dense assemblies of nanoparticles provides a powerful and potentially scalable approach to manufacture bio-inspired nanocomposites that mimic nacre's architecture. Solvent-driven infiltration of polymers (SIP) into nanoparticle packings formed on top of glassy polymer films is induced *via* capillary condensation of a solvent in the interstitial voids between nanoparticles (NP), followed by plasticization and transport of polymers into the liquid-filled pores, leading to the formation of the nanocomposite structure. To understand the effect of polymer–nanoparticle interactions on the dynamics of polymer infiltration in SIP, we perform molecular dynamics simulations. The mechanism of polymer infiltration and the influence of interactions between polymer and NPs on the dynamics of the process are investigated. Depending on the strength of interaction, polymer infiltration either follows (a) dissolution-dominated infiltration where plasticized polymer chains remain solvated in the pores and rapidly diffuse into the packing or (b) adhesion-dominated transport where the chains adsorb onto the nanoparticle surface and move slowly through the nanoparticle film as a well-defined front. A non-monotonic trend emerges as the adhesion strength is increased; the infiltration of chains becomes faster with the co-operative effect of adhesion and dissolution as adhesion increases but eventually slows down when the polymer–nanoparticle adhesion dominates.

Design, System, Application

In this study, molecular dynamics simulations are used to study the dynamics of infiltration of glassy polymers into solvent-filled NP packings. We find two modes of infiltration: a) a dissolution-dominated regime, in which solvent drives the polymer chains into the NP packing *via* dissolution due to the absence of strong interactions between polymer and NP surface, and b) an adhesion-driven regime, whereby strong interactions of the NP surface with the polymer induce infiltration of polymer *via* surface diffusion. By tuning the mutual interactions between the polymer, solvent and the NPs, the mechanism and the rate of infiltration can be controlled. A non-monotonic dependence of the rate on the strength of polymer–NP interactions is also shown. The fundamental understanding obtained in this study will enable optimization of processes to tailor the morphology of resulting nanocomposites through the molecular interactions which could be used in a wide range of applications including water filtration membranes, opto-electronic devices, and structural coatings.

Introduction

Nature provides numerous examples of nanocomposites that offer superb properties that far surpass the properties that are displayed by individual constituent materials or by currently-available synthetic composites. In particular, many natural composites exhibit cross-functionality. For example, the exceptional mechanical strength and toughness, two typically mutually exclusive properties of common materials, of naturally occurring composites like nacre (mother of pearl) have been attributed to the unique brick-and-mortar structure made by high loadings of platelets that form aligned layers interspersed by polymeric chains.[1–8] This powerful microstructure design improves adhesion of nanoparticles and imparts enhanced resistance to cracks by limiting direct routes for the crack to propagate within the material.[3,9–11] The toughness of bones and teeth in the

Department of Chemical and Biomolecular Engineering, University of Pennsylvania, Philadelphia, Pennsylvania 19104, USA. E-mail: kstebe@seas.upenn.edu, rrig@seas.upenn.edu, daeyeon@seas.upenn.edu

† Electronic supplementary information (ESI) available: Movies SM1–SM4. See DOI: 10.1039/c9me00148d

human body, as well as that of the cell wall in plants are similarly attributed to high concentration of anisotropic mineral materials that are aligned in a matrix of biopolymers such as cellulose and collagen.[3,4,11–14] Mollusk shells, arthropod cuticles, spicules of sponges and other tissues show a characteristic hierarchically assembled microstructure with a dominant ceramic phase supported by small volumes of organic matrix in between the inorganic phases. These examples show that achieving high loadings of nanoparticles is a promising strategy for producing nanocomposites with extraordinary properties and cross-functionality.

Although several methods have been developed to fabricate these bio-inspired nanocomposites, these approaches often require multiple processing steps, complex chemistry, and are time-consuming, making it difficult to enable continuous, large-scale manufacturing.[15–19] A promising way to circumvent these problems involves polymer infiltration into assemblies of nanomaterials.[20–25] This method takes advantage of the fact that a dense packing of nanomaterials can first be prepared, followed by polymer infiltration into the interstitial voids while retaining the arrangement and organization of the nanomaterials. Nanocomposites with extremely high fractions of nanomaterials bridged by small volumes of polymer can be fabricated this way. One effective way to induce infiltration of polymers into dense packings of nanoparticles is to use solvent vapor. In solvent-driven infiltration of polymer (SIP), a bilayer composed of a polymer layer underneath a dense packing of nanoparticles is exposed to solvent vapor. The solvent condenses in the nanoparticle packing *via* capillary condensation and the polymer film underneath is softened, leading to polymer infiltration into the liquid-filled pores of the nanoparticle packing. Any solvent that can condense in the pores of the packing and plasticize the underlying polymer film can be used to induce SIP. This method can be used with a wide range of polymers, nanoparticles and solvents, and can be tuned *via* the quality of solvent, duration of solvent exposure, and molecular weight of the polymer.[20] As long as the solvent is able to swell the underlying polymer layer, the mobilized polymer infiltrates into the nanoparticle packing.

The mode of polymer transport in the nanoparticle packings will likely have a significant impact on the dynamics of the infiltration process and the structure of nanocomposite that results from SIP. Thus, it is important to understand how the dynamics are affected by system parameters such as solvent quality, and the strength of polymer–nanoparticle interactions. A complete understanding of the dynamics of SIP will allow for more precise control over the manufacture and properties of the final composite material. Furthermore, the motion of polymer chains through these tortuous packings offers a rich system to study the motion and conformation of chains under extreme confinement. We note that the presence of solvent makes infiltration using SIP fundamentally different from capillary-driven infiltration[26,27] due to the numerous competing interactions (polymer–solvent, solvent–particle, polymer–particle) and expected increased role of entropic confinement. Experimental monitoring of SIP is challenging due to the rapid infiltration of polymers into the nanoparticle packing; similar values of the refractive index of the polymer and solvent-filled nanoparticle packing make optical characterization using ellipsometry difficult.

Molecular dynamics (MD) is a powerful approach to investigate the infiltration dynamics, because the interactions among different components (solvent, nanoparticle, polymer) can be tuned and the dynamics can be tracked with high precision. Equilibrium structure and diffusive dynamics of polymer nanocomposites have been well-studied using simulations before.[28–36] Monte Carlo, molecular dynamics and field theoretic techniques have been used to determine the role of graft chain density, chain length, matrix chain length, and matrix–particle interactions on the dispersion of nanoparticles in polymer melts. Several prior publications have also reported on polymer adsorption and diffusion on solid surfaces,[37–41] but few studies have investigated these phenomena in the context of fabricating polymer–nanoparticle composites and controlling their structures.

In this work, we will use MD techniques to investigate the dynamic process of polymer infiltration from a glassy film into the voids of a solvated nanoparticle packing. By varying the enthalpic interactions between the polymer and the nanoparticle, polymers can be induced to undergo dissolution-driven or adhesion-driven SIP. We detail the operation of these two modes and the difference in the dynamics in the two cases. The effect of the two mechanisms on the resulting structure of the composites is revealed by studying the chain conformations inside the packing after infiltration. This study sheds light on the parameters that control these two different infiltration mechanisms and their impact on the infiltration of polymers under confinement. The dynamical understanding gained from this study can further be used for the scale-up of this process to enable scalable manufacturing of highly loaded nanocomposite films and membranes.

Methods

A coarse-grained model that reflects the experimental system is developed to capture the essential physics underlying SIP as explained below. These coarse grained models reduce the complexity of the actual system by lumping atomistic details while retaining the relevant physics behind the process and are similar to the ones used in many previous studies.[26–28,30,42,43]

System design

Our simulation box is periodic in x and y but not in z, as shown in Fig. 1(a). A freely rotating chain model is chosen for the polymer with backbone rigidity built into the chain to avoid polymer–solvent co-crystallization at low temperatures. Each polymer chain has $N = 20$ Lennard Jones (LJ) beads that

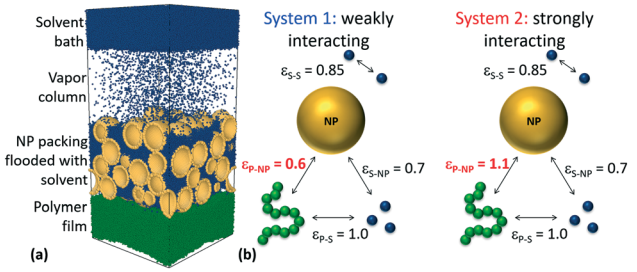

Fig. 1 (a): Model system for SIP, (b): choice of interaction potential among the different species in the model system.

are held together by FENE (finitely extensible non-linear elastic) bonds acting between pairs of adjacent monomers with the potential described by:[44–46]

$$U_{ij}^{b} = -0.5KR_0^2 \ln\left(1-\left(\frac{r}{R_0}\right)^2\right) + 4\varepsilon\left[\left(\frac{\sigma}{r}\right)^{12} - \left(\frac{\sigma}{r}\right)^{6}\right] + \varepsilon \quad (1)$$

where i, j are adjacent monomers and b refers to the bonded interaction between them. In our simulations $K = 30\varepsilon/\sigma^2$, $R_0 = 1.5\sigma$ and the LJ energy ε and diameter σ are taken as unity. The angles between adjacent bonds are maintained at 120 degrees by an angular harmonic potential of the form

$$U_{\text{ang}} = \frac{K_\theta}{2}(\theta-\theta_0)^2 \quad (2)$$

where K_θ is the strength of this interaction and θ_0 is the equilibrium bond angle. We choose to work with $K_\theta = 20\varepsilon/\text{radian}^2$ and $\theta_0 = 120$ degrees. The previously reported glass transition temperature of this model polymer is $T_g = 0.66$ (ref. 47) which we verify through an independent simulation. All quantities reported are in LJ units – unit of length is in σ of the monomer, unit of energy is in ε of the interaction between two monomers, and mass is in the units of mass of a monomer m. All the other units follow from these LJ units such that the unit of temperature is ε/K_B.

Non-bonded particles interact with each other *via* standard 12–6 LJ truncated and modified potential:

$$U_{ij}^{\text{nb}} = 4\varepsilon_{ij}\left[\left(\frac{\sigma}{r_{ij}}\right)^{12} - \left(\frac{\sigma}{r_{ij}}\right)^{6}\right] - 4\varepsilon_{ij}\left[\left(\frac{\sigma}{r_{\text{cut}}}\right)^{12} - \left(\frac{\sigma}{r_{\text{cut}}}\right)^{6}\right] \quad (3)$$

where the superscript nb specifies the non-bonded nature of the interaction. The cutoff radius is set at 2.5σ; ε and σ are set to 1 for monomer–monomer interactions. To start the simulation with a glassy polymer film, we set the working temperature for our simulation as $T = 0.6$ ($T/T_g \approx 0.91$). The chain length chosen ($N = 20$) such that these chains behave as unentangled chains. The average radius of gyration of the chains in the glassy film is 2.5σ units.

The free-standing polymer films were generated by randomly growing polymers inside a rectangular box with periodic boundaries in x and y directions. After placing the polymers in the box, we used soft potential at first to push away overlapping monomers, and then we switched to the standard LJ potential for equilibration with Nosé–Hoover thermostat (NVT) at $T = 0.7$ (until the mean squared displacements of the monomers indicate diffusive behaviour). During the equilibration, we used a large box in the z-direction to achieve free standing films. To obtain glassy polymer films, we cool the polymer films to $T = 0.6$ at a specific cooling rate of $\Delta T/\Delta t = 1.0$ per $2000\tau_{\text{LJ}}$. The thickness of the polymer film is approximately 34.5σ in the z-direction and 75σ in the x- and y-directions. The film is aged for an additional $400\,000\tau_{\text{LJ}}$ of NVT integration at $T = 0.6$ so there is no aging on the time scale of the infiltration simulations.

The nanoparticle (NP) packing consists of 56 NPs, and we model each NP as hollow shell comprised of approximately 1000 LJ beads which are placed along a spherical surface with predetermined radius and each LJ bead occupies around $1\sigma^2$ unit area on the surface. The NPs are polydisperse and their diameter varies from approximately 15σ–20σ with a mean value of 17.5σ with a standard deviation of 1σ. To achieve randomly packed NPs, we place all the NPs in a very large simulation box where NPs are highly dispersed. Initially, we equilibrate the system with NVT at $T = 5.0$ for $2000\tau_{\text{LJ}}$ and after equilibration, we deform the simulation box over $200\tau_{\text{LJ}}$ in both x and y dimensions to our final desired box dimension of $L_x = L_y = 75\sigma$. Lastly, we cool the NPs system from $T = 5.0$ to our desired temperature $T = 0.6$ over $2000\tau_{\text{LJ}}$, meanwhile we apply a force in the negative z direction of 0.05 to condense the NPs along the z axis onto a smooth wall at the bottom z edge of the box. In the end, the packing fraction of the system is ≈0.6 (vol NPs/vol box). After creating the dense NP film, the NPs are held fixed throughout the simulation; previous simulations of infiltrated nanoparticle packings with a similar model has shown that the particles do not separate if we relax this constraint.[26]

The solvent is made up of LJ particles with self-interactions between the monomers chosen such that a vapor column and a solvent bath are both stable at $T = 0.6$. For the standard 12–6 LJ truncated and shifted potential described by eqn (2), $\varepsilon = 0.85$, $\sigma = 1.0$ and a cutoff applied at 2.5σ at $T = 0.6$ satisfies the co-existence of the solvent and vapor phases.

In experimental realizations of SIP, the polymer–NP bilayer is exposed to a solvent vapor following which the solvent floods the NP packing by capillary condensation. We replicate this experimental phenomenon by setting up the initial configuration of the system as a NP packing filled with liquid solvent along with a vapor solvent column above it and a polymer film beneath it, as shown in Fig. 1. This vapor column of thickness 80σ and average density $0.0081\sigma^{-3}$ is placed on top of the packing and is continuously replenished by a 20σ thick solvent bath on top. The solvent bath is held to the top of the simulation box by a weak LJ interaction with the plane at the top of the simulation box, which is governed by the following potential:

$$U_{ij}^{\text{wall}} = \varepsilon\left[\frac{2}{15}\left(\frac{\sigma}{r}\right)^9 - \left(\frac{\sigma}{r}\right)^3\right] \quad (4)$$

with ε = 1.0 between the wall and the solvent monomers, σ = 1.0 and the cutoff is applied at 2.5σ units. Periodic boundary conditions are used in the *xy*-plane.

The solvent condensed within the packing, in the vapor column and in the solvent bath is held at T = 0.6 for 2000τ_{LJ} time to ensure that the system reaches equilibrium as verified by monitoring the total energy of the system which reaches a steady value. The entire system of the solvated NP packing, polymer film and vapor column with more than 400 000 LJ interaction sites is shown in Fig. 1(a). The polymer film is initially placed 1σ below the solvated nanoparticle packing before SIP is initiated, and during the simulation the NP positions are held fixed.

Choice of interaction coefficients

The mutual interactions between the solvent, NPs and the polymer monomers and their respective self-interactions are all governed by the modified and truncated LJ potential with a cutoff of 2.5σ units. The choice of ε or the strength of the interaction in the LJ potential is governed by the physics that we seek to simulate. The self-interaction for the monomers in the polymer chain sets the basis for choosing other interactions, and thus the ε between non-bonded polymer monomers is set at 1.0. The mutual interactions between the solvent in both the vapor and the liquid states are 0.85 which ensures that both the vapor and the liquid states will coexist at T = 0.6. The self-interaction between the LJ sites that comprise the NP surfaces is set to 1.0.

The interaction potential between the solvent and the polymer determines the solvent quality for the polymer. In a good solvent with a large ε_{P-S} ($<(\varepsilon_{P-P} + \varepsilon_{S-S})/2$), the polymer adopts an expanded chain conformation, whereas in a poor solvent with a smaller value of ε_{P-S} ($>(\varepsilon_{P-P} + \varepsilon_{S-S})/2$), the polymer collapses or is barely solvated, which potentially favours its partitioning to the NP surface. To relate these interaction parameters to the Flory–Huggins interaction parameter χ, which represents the degree of enthalpic interactions between two components (in this case, polymer and solvent), we use ε_{P-S} = 1, which corresponds to a good solvent condition given the smaller magnitude of ε_{S-S}. This allows for net interactions between the solvent and the polymer monomers to be more attractive than the mutual interactions between the solvent monomers. The solvent monomers and the NPs interact with a coefficient of 0.7 which is chosen so that the solvent has more affinity for the polymer chains than to the NPs.

The polymer–NP interaction (ε_{P-NP}) is chosen to be either 0.6 or 1.1 while all the other interaction coefficients are kept constant to design two systems that probe the effect of varying polymer–NP interactions while maintaining constant solvent quality, as illustrated in Fig. 1(b). We define the system with ε_{P-NP} = 0.6 as the weakly interacting system where the most favorable interactions in the system are between the solvent and the polymer, and there are relatively weak interactions between the NP and the polymer. When ε_{P-NP} = 1.1, we have a strongly interacting system in which the polymers are strongly attracted to the NP surface. These simulations are then expected to provide insight on the differences in behavior when the polymer has preferential interactions with the solvent *versus* with the NPs.

Simulation details

Molecular dynamics simulations for the two systems are performed at T = 0.6 with a timestep of 0.002 LJ time units using the LAMMPS software package.[48] The weakly interacting system is run for 800 000τ_{LJ} whereas the strongly interacting system is run for 1 600 000τ_{LJ}. The NPs are held fixed in both systems. A control MD simulation is performed of the bilayer structure of polymer and NPs absent solvent. The polymer does not infiltrate into the packing which is consistent with the experimental finding that the glassy polymer film needs to be plasticized by the solvent before any infiltration can take place.

Results and discussions

Infiltration of polymers into the interstices of the nanoparticle packing is observed in both the weakly and strongly interacting systems within 200τ_{LJ}. A 3-D visualization of the trajectory of the simulated system shows that the polymer film is first plasticized by the incoming solvent, which gives the chains mobility to move up through the pores in the packing (refer to Movies SM1–SM4 provided in the ESI†). The bulk motion of solvent and polymers can be monitored *via* density plots which show the number density of the solvent and the polymer monomers in bins of unit height along the *z* direction.

Fig. 2(a) and (b) show the evolution of the density profiles of polymer and solvent (ρ_P and ρ_S) in the weakly interacting system within the NP packing (the top and bottom of the nanoparticle packing is shown using dashed lines). The regular oscillations in the density profiles are due to the liquid-like packing of nanoparticles at the interface, which leads to oscillations in the available void volume. At t = 0, the dense polymer film rests at the bottom of the packing and the solvent exists as liquid in the packing and as vapor in the region above. Upon the initiation of the simulation (*i.e.*, the polymer film is brought into contact with the liquid-filled NP packing), the solvent moves into the glassy polymer film and diffuses through the polymer film until the polymer is completely solvated. Simultaneously, the polymer chains that have gained mobility during this solvation process rapidly advance into the packing. We also see interesting effects in the vapor phase and the solvent film covering the tops of the nanoparticles. Initially, the interstitial solvent gets depleted as the solvent leaves the packing to solvate the polymer film; however, the liquid-phase solvent within the packing is replenished rapidly *via* condensation from the vapor phase. This can be seen by the increase in the solvent density on the top of the packing at t = 200 000τ_{LJ}. Consequently, the

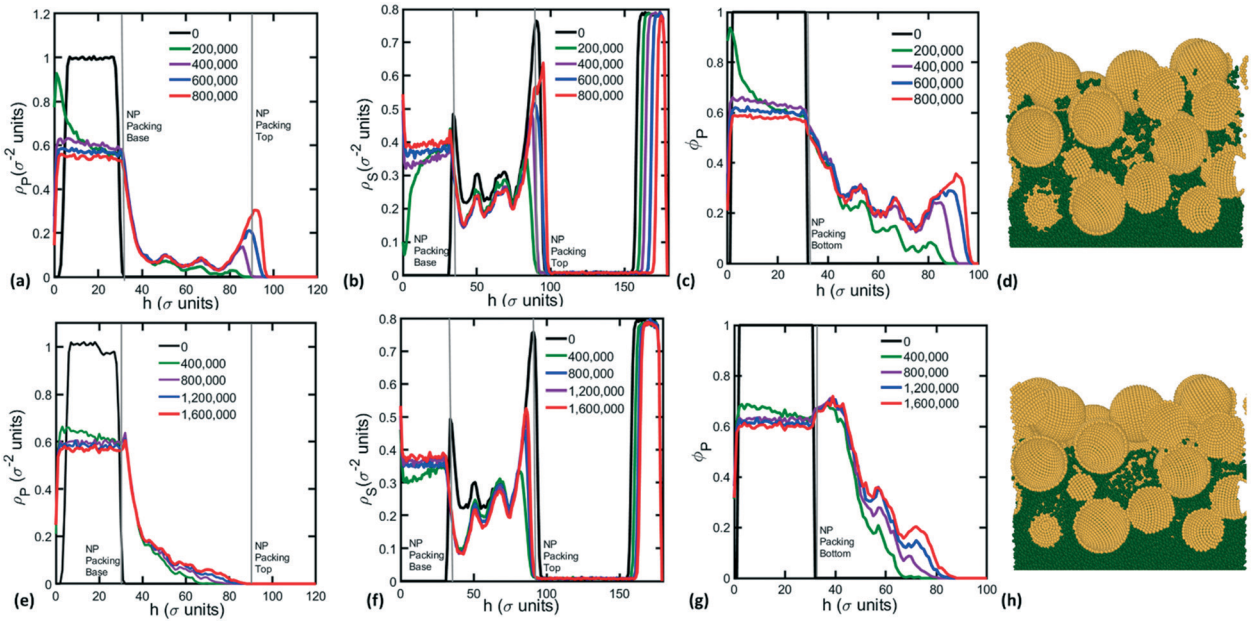

Fig. 2 (a) Density of weakly interacting (ε_{P-NP} = 0.6, T = 0.6) polymers along the z-direction, (b) density of solvent monomers along the z-direction in the weakly interacting system (ε_{P-NP} = 0.6, T = 0.6), (c) concentration of polymer along the z-direction in the weakly interacting system (ε_{P-NP} = 0.6, T = 0.6), (e) density of strongly interacting polymers (ε_{P-NP} = 1.1, T = 0.6) along the z-direction, (f) density of solvent monomers along the z-direction in the strongly interacting system (ε_{P-NP} = 1.1, T = 0.6), (g) concentration of polymer along the z-direction in the strongly interacting system (ε_{P-NP} = 1.1, T = 0.6). Legends in all figures (a)–(c) and (e)–(g) show the time (in τ_{LJ} units) at which the data is obtained. The top and base of the packing are indicated by dashed lines in all the figures, snapshots of (d) weakly interacting system (ε_{P-NP} = 0.6, T = 0.6) and (h) strongly interacting system (ε_{P-NP} = 1.1, T = 0.6).

thickness of the solvent bath above the vapor film continues to decrease. At 800 000τ_{LJ}, the density of the polymer in the packing stops changing at which point the simulation is terminated. Any additional polymers going into the packing beyond this time is due to the presence of a thin solvent film that forms atop the nanoparticle packing.

The density profiles for the polymer and the solvent in the strongly interacting system are shown in Fig. 2(e) and (f). The polymer moves far more slowly into the nanoparticle packing than it does in the weakly interacting system; even at the end of 1 600 000τ_{LJ}, polymer infiltration has not ceased. The simulation up to this point provides sufficient information for us to understand the dynamics of polymer infiltration. We therefore stop the simulation at 1 600 000τ_{LJ}, despite the system not yet reaching maximum infiltration.

To directly compare the infiltration dynamics of polymers in the two systems, temporal evolution of polymer concentration inside the packing is inferred from the density profiles using the mole fraction of the polymer in the solution.

$$\phi_P = \frac{\text{density of polymer}}{\text{density of polymer} + \text{density of solvent}} = \frac{\rho_P}{\rho_P + \rho_S}$$

In the weakly interacting system (Fig. 2(c)), the infiltrating polymers spread out inside the packing as a diffuse front and this diffuse concentration profile develops over time into a "steady" profile which shows alternating regions of high and low concentrations inside the packing. Experimental work has shown that no clear infiltrating front could be observed using ellipsometry,[20] which agrees with the absence of a clear front simulated here. The chains dissolved in the solvent distribute rapidly in the void space throughout the packing, preventing development of a sharp front. The overall concentration of the polymer increases over time, and the final distribution of polymers shows that the chains are concentrated more in the regions with greater void space in the packing. This distribution provides insight into the effect of confinement on solubility. That is, polymers prefer to partition into less confining voids within the packing.

The strongly interacting system (Fig. 2(g)), in contrast, shows a clear, well-defined front that moves through the particle packing in time instead of spreading out over the entire packing. A sharp increase in the polymer concentration near the bottom of the nanoparticle packing also is observed. At the initial stage of infiltration, the polymer film moves close to the bottom of the packing, owing to strong interactions between the polymer and the nanoparticle, and nearly plugs the voids near the bottom of the packing. This explains the peak in monomer density near the bottom of the packing.

Local environment around the polymers: elucidating the difference in the two mechanisms

The density profiles show that the polymer infiltration in the two systems occurs at different rates and distributions. In the weakly interacting system, chains move in rapidly and spread throughout the entire packing whereas in the strongly interacting system, chains move up very slowly with a relatively cohesive front. These differences in the polymer

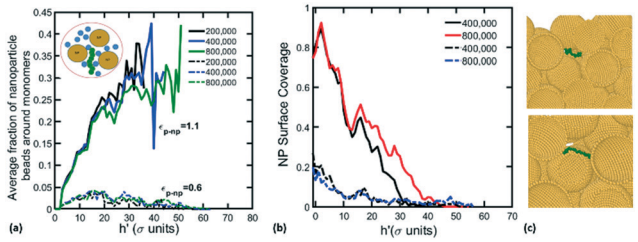

Fig. 3 (a) Average fraction of nanoparticle beads at a distance of 1.5σ from monomers in the strongly ($\varepsilon_{P\text{–}NP}$ = 1.1, T = 0.6 – thick lines) and weakly interacting systems ($\varepsilon_{P\text{–}NP}$ = 0.6, T = 0.6 – dashed lines) plotted against distance from the base of the packing h' (shown in the inset is a representation of the shell used to count the nanoparticle beads; the nanoparticles are shown to be smaller than their actual size in the system), (b) average surface coverage of nanoparticles in the packing as a function of the distance from the base of the packing (h') in the strongly ($\varepsilon_{P\text{–}NP}$ = 1.1, T = 0.6 – thick lines) and weakly interacting systems ($\varepsilon_{P\text{–}NP}$ = 0.6, T = 0.6 – dashed lines), (c) snapshots from simulations show the two mechanistic routes of infiltration of polymers; legend in (a) and (b) indicate time (in τ_{LJ} units) at which data is taken.

chain motion come from different paths taken by the chains as revealed by analyzing the local environment around each chain.

Fig. 3(a) shows the average fraction of nanoparticle surface beads out of the total number of LJ monomers (solvent, nanoparticle surface, and polymeric monomers) within 1.5σ distance of each monomer. The monomers in the strongly interacting system (thick lines) are surrounded more by nanoparticle beads than by solvent molecules or other polymer monomers. In contrast, the weakly interacting chains (dashed lines) have far fewer nanoparticle beads in the shells around them and are enveloped more by solvent molecules. The data can also be represented as average coverage of nanoparticle surface beads by polymer monomers at varying heights, as seen in Fig. 3(b). The nanoparticles in the strongly interacting system have substantially greater coverage of polymer monomers compared to those in the weakly interacting system.

Together, the data on surface coverage of nanoparticles and the local environment around each chain differentiate the two routes taken by chains to infiltrate into the packing (Fig. 3(c)):

1. Dissolution-dominated pathway in the weakly interacting system: the strong interactions between the solvent and the polymer in this case induce the polymers to move up through the packing by "*swimming*" inside the solvent environment. The chains have little contact with the nanoparticles and the primary driving force is the chemical potential gradient due to the concentration differences within the packing.

2. Adhesion-dominated pathway in the strongly interacting system: here, the strongest interactions are between the polymer and the nanoparticle. The interaction between nanoparticles and polymer provides a driving force for the polymer chains to move up inside the packing by surface diffusion. The chains are adsorbed on the surface of the nanoparticles and move forward by surface-diffusion mediated "*crawling*".

Relative rates of infiltration: the influence of mechanism on the dynamics of infiltration

As discussed above, the two mechanisms offer distinct routes for the polymers to infiltrate into the nanoparticle packing. The two pathways not only differ in the environment around the chains in the packing but also in the respective dynamics of the infiltration process. Careful analyses of the concentration profiles gives us insight into the reason behind the different rates as shown in Fig. 4(a). The concentration profiles in the weakly interacting case show that the chains spread out throughout the packing in the form of a diffuse front which does not move any further but develops over time. In the strongly interacting case, the chains infiltrate in the form of a sharp front which moves forward with time.

Another difference that can be seen is the location of peaks in the concentration of polymer in the packing (Fig. 4). The profiles for the weakly interacting system have well-defined peaks in the packing which correlate with regions of higher void volume. The weakly interacting chains tend to accumulate in these larger interstitial pockets in the packing, likely to minimize the entropic penalty from confinement. In contrast, the profiles for the strongly interacting system show peaks that are anti-correlated with the void volume of the packing. Regions where nanoparticles are closer together and form constrictions have greater surface area for the crawling chains to adsorb onto.

This difference in dynamics can be quantitatively analyzed by tracking the infiltration front inside the packing and the thickness of this advancing front which can be obtained by integrating the density profiles to find the point at which 85% (H_{85}) and 99% (H_{99}) of the monomers are found. The dynamics of infiltration in the weakly interacting system are much faster than the strongly interacting case as seen by

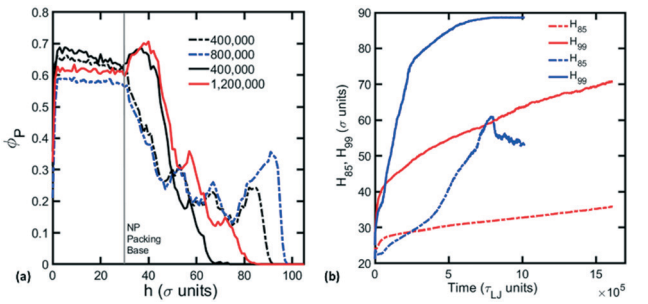

Fig. 4 (a) Concentration profiles for the N = 20 weakly ($\varepsilon_{P\text{–}NP}$ = 0.6, T = 0.6 – dashed lines) and strongly interacting systems ($\varepsilon_{P\text{–}NP}$ = 1.1, T = 0.6 – thick lines). The data for each curve has been obtained by averaging data front an interval of width 100 000τ_{LJ} centered around the time (in τ_{LJ}) marked in the legend, (b) front position indicators H_{85} and H_{99} for the two systems – blue curves depict data for weakly ($\varepsilon_{P\text{–}NP}$ = 0.6, T = 0.6) interacting system and the red curves depict data for strongly interacting systems ($\varepsilon_{P\text{–}NP}$ = 1.1, T = 0.6). Dashed line marks the base of the packing in (a).

comparing the slopes of the respective H_{85} or H_{99} curves in Fig. 4(b). More careful comparison reveals important differences between these two different systems. The chains on top of the packing in the weakly interacting system form a thin layer of polymer solution with the condensing vapor once the packing has been completely filled. To eliminate this phenomenon from affecting the analysis during infiltration, we calculate the H_{85} and H_{99} using a cutoff applied at the top for the weakly interacting system. This explains the gradual saturation in the infiltration heights H_{85} and H_{99} after $800\,000\tau_{LJ}$.

Comparing the rate of change of H_{99} which is the point of location of the highest polymers in the two cases (thick blue and red curves), we see that in the weakly interacting system, the chains reach the top of the packing quite rapidly. In contrast, in the strongly interacting system, the chains gradually rise up in the packing; that is, there is a region that remains completely free of chains that is gradually filled up from the bottom to the top. This difference in behavior of the fastest chains signals the presence of a cohesive front in the case of the strongly interacting system. The H_{85} curves for the two systems (shown as dashed curves in red and blue) mark the point at which the bulk of the polymers reside. Once again, there is a difference in dynamics in the two cases where we see the weakly interacting chains filling a large fraction of the packing quite rapidly whereas the strongly interacting chains reside mostly in the lower part of the packing ($29.5\sigma < z < 35\sigma$).

To analyze the dependence of the rate of infiltration on the interaction strength between nanoparticles and polymers $\varepsilon_{P\text{–}NP}$, we carry out additional simulations in which the infiltration is performed at a higher temperature, and where the interaction between the nanoparticles and the polymers $\varepsilon_{P\text{–}NP}$ is varied from 0.6 to 1.5. To facilitate the equilibration of the polymer film prior to infiltration and to enhance the infiltration dynamics, T = 0.7, above the T_g of the polymer. The infiltration process is initiated once the solvent completely fills the interstices of the packing. We use a version of our polymer model with faster dynamics, with N = 20, a harmonic bonding potential $U_{ij}^{b} = \frac{k_h}{2}(r_{ij}-\sigma)^2$, where k_h = 200, and the angle potential is removed (K_θ = 0). Non-bonded monomers interact through a standard 12–6 LJ truncated and shifted potential with a cut-off radius of 2.5σ. The interactions among nanoparticles, as well as polymers and solvent, are kept the same as the previous simulations; that is $\varepsilon_{S\text{–}S}$ = 1.0, $\varepsilon_{P\text{–}P}$ = 1.0, $\varepsilon_{NP\text{–}NP}$ = 1.0. The interaction between the solvent and polymers is set as $\varepsilon_{S\text{–}P}$ = 1.0 and the interaction between the solvent and nanoparticles is $\varepsilon_{S\text{–}NP}$ = 0.7. We observe a non-monotonic dependence of the infiltration process on the interaction between nanoparticles and polymers $\varepsilon_{P\text{–}NP}$ as shown in Fig. 5. For both $H_{99}^2(t)$ and $H_{85}^2(t)$ plotted in Fig. 5(a) and (b) with different $\varepsilon_{P\text{–}NP}$, during early stages (time $< 10^4\ \tau_{LJ}$) all the systems show a quick front motion of the polymer films as the polymer wets the bottom of the NP films. This initial wetting is followed by an almost linear increase in the front position as infiltration processes are observed. As $\varepsilon_{P\text{–}NP}$ increases from 0.5 to 1.0, the infiltration process transitions from a dissolution-driven process to a surface-dominated process; the infiltration rate increases due to the combined effect of favorable interactions of polymer with both solvent and NP. However, as $\varepsilon_{P\text{–}NP}$ is further increased from 1.0 to 1.5, the surface interaction between the nanoparticles and the polymers is too strong such that the rate of infiltration decreases; that is the infiltration process slows down with an increase in epsilon in both plots of H_{99}^2 and H_{85}^2. To show these trends more clearly, we plot H_{99}^2 and H_{85}^2 as a function of $\varepsilon_{P\text{–}NP}$ at different time points in Fig. 5(c) and (d). The heights of the infiltrating fronts increase as $\varepsilon_{P\text{–}NP}$ increases from 0.6 to 1.0 and peak at $\varepsilon_{P\text{–}NP}$ = 1.0, then decrease as $\varepsilon_{P\text{–}NP}$ is further increased from 1.0 to 1.5 for all the time points. This trend is more obvious at long time scales such as $t = 30\,000\tau_{LJ}$ and $t = 50\,000\tau_{LJ}$. As the interaction $\varepsilon_{P\text{–}NP}$ between nanoparticles and polymers is increased, the friction between the polymer monomers and the surface of the nanoparticles increases substantially and dominates the behavior as $\varepsilon_{P\text{–}NP}$ increases from 1.0 to 1.5. No polymers move up through the solvent, and thus it takes longer time for the strongly adhered polymers to climb up *via* surface diffusion. These results provide important insight into how adjusting the interaction between polymers and nanoparticles can control the rate of the SIP process.

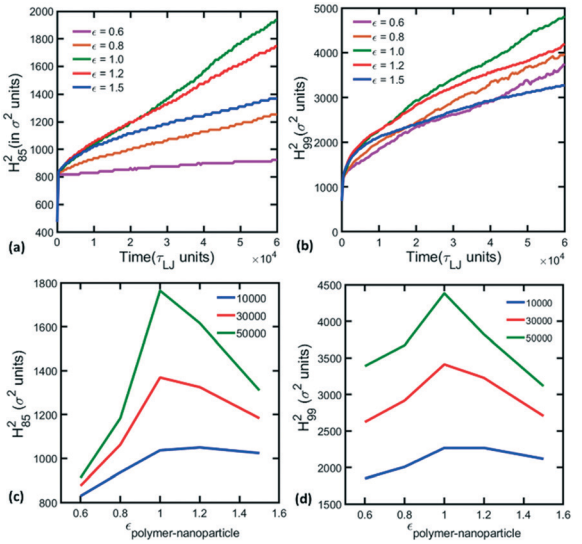

Fig. 5 H_{99}^2 and H_{85}^2 are plotted as a function of time with different polymer and nanoparticle interaction $\varepsilon_{P\text{–}NP}$ from 0.6 to 1.5 in (a) and (b) at T = 0.7. At three different time (indicated in legend in τ_{LJ} units), H_{99}^2 and H_{85}^2 are plotted as a function of polymers and nanoparticle interaction $\varepsilon_{P\text{–}NP}$ in (c) and (d) at T = 0.7.

Local conformation within the packing

The mechanism of infiltration of polymers into the packing affects the dynamics of the infiltration process due to the different local environments around polymers in each case. Whether a chain is solvated in the void region or adsorbed

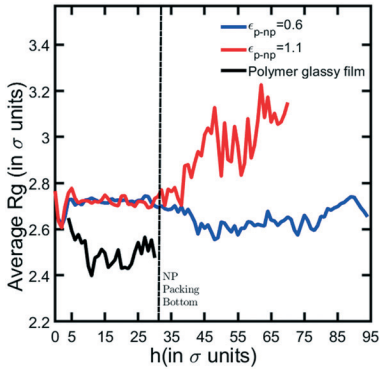

Fig. 6 Radius of gyration (R_g) of polymer chains averaged in bins of 1σ width in the z direction plotted as a function of distance from the base of the simulation box (h). The data for both systems was averaged over 100 frames at equal intervals from t = 750 000τ to t = 850 000τ. Dashed line shows the point where the packing begins. This is done on the results obtained for the system at T = 0.6.

on the nanoparticle surface affects the local structure of chains inside the packing which ultimately affects the structure and properties of the final nanocomposite films made using SIP. We analyze the conformation of polymers inside the packing by characterizing the average chain size at different locations within the packing. The nanoparticle packing is split into bins of uniform size of 0.5σ. For each bin, the radius of gyration of chains (R_g) of any polymer whose center of mass lies in the bin is calculated and the R_g value is obtained by averaging over all polymers in the bin. Fig. 6 shows the average chain sizes obtained for both the strongly and the weakly interacting systems, as well as the average chain size in the glassy film below the packing, at t = 0 and the subsequent increase in the chain size due to solvation of the film.

The weakly interacting chains in the packing are smaller than chains in the solvated film, as seen in the shift in the red curves towards smaller sizes upon entering the packing (right of dashed line in Fig. 6) as compared to the red curve representing chains in the swollen polymer film (left of dashed line). This trend shows the effect of confinement on the chains; that is, the chains contract to fit into the small interstices between the nanoparticles. In contrast, chains in the strongly interacting system spread out on the nanoparticle surface and thus have a larger average radius of gyration (blue curve) when compared to both the weakly interacting chains and the solvated films. The strongly interacting chains are not affected the same way as the weakly interacting chains as they do not experience the same three-dimensional confinement that the small interstitial pores are imposing on the weakly interacting chains. These results may have important implications on the mechanical properties of the SIP nanocomposites. For example, extended chain dimensions in the strongly interacting system could potentially lead to bridging of nanoparticles by the chains which would strengthen and toughen the nanoparticle packings.[49]

Conclusions

Using molecular dynamics simulations, we have studied the effect of the polymer–nanoparticle interaction on the mechanism and dynamics of SIP. By adjusting the relative strength of pair interactions between the solvent, polymer and nanoparticles, we observe two distinct modes of infiltration: dissolution-dominated and adhesion-dominated. In the dissolution-driven mechanism, the polymers infiltrate as a diffuse front and move more rapidly than in the adhesion-driven case where the adsorbed polymers move forward as a cohesive front. By varying the strength of interactions between the polymer and the nanoparticle, we show that the infiltration dynamics become faster with increasing interaction until a strong-adhesion limit, beyond which infiltration slows down.

Both systems offer rich insights into solvated polymer motion under confinement. The dissolution-driven mechanism can be used as an ideal system to study entropic barriers in geometries with complex topography. In fact, similar mechanisms have been used to describe the separation and transport of DNA molecules in microchannels and other confined environments.[50–52] The adhesion-driven systems are not as affected by the physical confinement as are the dissolution-driven systems, but the strength of interactions can have substantial and non-monotonic influence on the rate of infiltration. The effect of molecular weight of the polymer on the infiltration dynamics is the focus of our on-going studies. Preliminary simulations on SIP of high molecular weight (N = 50) polymers with weak polymer–nanoparticle interactions have shown that infiltration slows down considerably as the polymer becomes larger. Future work will be directed at understanding the effect of the interactions of polymer and nanoparticles on the final structure of the composite as well as the local segmental dynamics of chains during infiltration. In particular, previous studies on polymer adsorption have reported a first-order phase transition that results in discontinuous adsorption and desorption of the polymer.[53,54] Further investigation into the role of such a transition on the dynamics and structure of SIP nanocomposites will be conducted. We believe the different structures that can result from SIP nanocomposites produced *via* different infiltration pathways can have a wide range of applications in membrane separations as well as structural coatings.

Conflicts of interest

There are no conflict of interests to declare.

Acknowledgements

This work was supported by Penn MRSEC (NSF DMR 1720530) and NSF CBET-1933704 and computational resources were provided through XSEDE award TG-DMR150034.

Notes and references

1 F. Barthelat, H. Tang, P. D. Zavattieri, C. M. Li and H. D. Espinosa, *J. Mech. Phys. Solids*, 2007, **55**, 306–337.
2 E. Manias, *Nat. Mater.*, 2007, **6**, 9–11.
3 H. Gao, B. Ji, I. L. Jäger, E. Arzt and P. Fratzl, *Proc. Natl. Acad. Sci. U. S. A.*, 2003, **100**, 5597–5600.
4 F. Bouville, E. Maire, S. Meille, B. Van De Moortèle, A. J. Stevenson and S. Deville, *Nat. Mater.*, 2014, **13**, 508–514.
5 G. Mayer, *Science*, 2005, **310**, 1144–1147.
6 P. Peças, H. Carvalho, H. Salman and M. Leite, *J. Compos. Sci.*, 2018, **2**, 66.
7 B. Chen and J. R. G. Evans, *J. Phys. Chem. B*, 2004, **108**, 14986–14990.
8 U. G. K. Wegst, H. Bai, E. Saiz, A. P. Tomsia and R. O. Ritchie, *Nat. Mater.*, 2015, **14**, 23–36.
9 S. G. Isaacson, Y. Matsuda, K. Lionti, T. Frot, W. Volksen, R. H. Dauskardt and G. Dubois, *ACS Appl. Mater. Interfaces*, 2018, **10**, 27549–27554.
10 L. J. Bonderer, A. R. Studart and L. J. Gauckler, *Science*, 2008, **319**, 1069–1073.
11 D. Sen and M. J. Buehler, *Sci. Rep.*, 2011, **1**, 35.
12 H. D. Wagner and S. Weiner, *J. Biomech.*, 1992, **25**, 1311–1320.
13 M. Alexandre and P. Dubois, *Mater. Sci. Eng., R*, 2000, **28**, 1–63.
14 E. Munch, M. E. Launey, D. H. Alsem, E. Saiz, A. P. Tomsia and R. O. Ritchie, *Science*, 2008, **322**, 1516–1520.
15 P. Akcora, H. Liu, S. K. Kumar, J. Moll, Y. Li, B. C. Benicewicz, L. S. Schadler, D. Acehan, A. Z. Panagiotopoulos, V. Pryamitsyn, V. Ganesan, J. Ilavsky, P. Thiyagarajan, R. H. Colby and J. F. Douglas, *Nat. Mater.*, 2009, **8**, 354–359.
16 T. Gatti, N. Vicentini, M. Mba and E. Menna, *Eur. J. Org. Chem.*, 2016, **6**, 1071–1090.
17 R. M. Erb, J. S. Sander, R. Grisch and A. R. Studart, *Nat. Commun.*, 2013, **4**, 1712.
18 W. Benhadjala, M. Gravoueille, I. Bord-Majek, L. Béchou, E. Suhir, M. Buet, M. Louarn, M. Weiss, F. Rougé, V. Gaud and Y. Ousten, *Appl. Phys. Lett.*, 2015, **107**, 211903.
19 S. Cheng and G. S. Grest, *ACS Macro Lett.*, 2016, **5**, 694–698.
20 N. Manohar, K. J. Stebe and D. Lee, *ACS Macro Lett.*, 2017, **6**, 1104–1108.
21 P. E. De Jongh and T. M. Eggenhuisen, *Adv. Mater.*, 2013, **25**, 6672–6690.
22 Y. R. Huang, Y. Jiang, J. L. Hor, R. Gupta, L. Zhang, K. J. Stebe, G. Feng, K. T. Turner and D. Lee, *Nanoscale*, 2015, **7**, 798–805.
23 J. L. Hor, Y. Jiang, D. J. Ring, R. A. Riggleman, K. T. Turner and D. Lee, *ACS Nano*, 2017, **11**, 3229–3236.
24 Y. Qiang, N. Manohar, K. J. Stebe and D. Lee, *Mol. Syst. Des. Eng.*, 2018, **3**, 96–102.
25 R. B. Venkatesh, S. H. Han and D. Lee, *Nanoscale Horiz.*, 2019, **4**, 933–939.
26 A. Shavit and R. A. Riggleman, *Soft Matter*, 2015, **11**, 8285–8295.
27 D. J. Ring, R. A. Riggleman and D. Lee, *ACS Macro Lett.*, 2019, **8**, 31–35.
28 D. Meng, S. K. Kumar, S. Cheng and G. S. Grest, *Soft Matter*, 2013, **9**, 5417–5427.
29 T. V. M. Ndoro, E. Voyiatzis, A. Ghanbari, D. N. Theodorou, M. C. Böhm and F. Müller-Plathe, *Macromolecules*, 2011, **44**, 2316–2327.
30 F. Lo Verso, L. Yelash, S. A. Egorov and K. Binder, *J. Chem. Phys.*, 2011, **135**, 214902.
31 F. W. Starr, T. B. Schrøder and S. C. Glotzer, *Macromolecules*, 2002, **35**, 4481–4492.
32 M. Vacatello, *Macromolecules*, 2001, **34**, 1946–1952.
33 J. Liu, Y. Wu, J. Shen, Y. Gao, L. Zhang and D. Cao, *Phys. Chem. Chem. Phys.*, 2011, **13**, 13058.
34 J. Koski, H. Chao and R. A. Riggleman, *J. Chem. Phys.*, 2013, **139**, 244911.
35 J. Koski, H. Chao and R. A. Riggleman, *Chem. Commun.*, 2015, **51**, 5440–5443.
36 R. B. Thompson, V. V. Ginzburg, M. W. Matsen and A. C. Balazs, *Science*, 2001, **292**, 2469–2472.
37 T. G. Desai, P. Keblinski, S. K. Kumar and S. Granick, *Phys. Rev. Lett.*, 2007, **98**, 1–4.
38 C. J. Bradly, A. L. Owczarek and T. Prellberg, *Phys. Rev. E*, 2019, **99**, 1–5.
39 P. H. L. Martins, J. A. Plascak and M. Bachmann, *J. Chem. Phys.*, 2018, **148**, 1–9.
40 C.-Y. Li, W.-P. Cao, M.-B. Luo and H. Li, *Colloid Polym. Sci.*, 2016, **294**, 1001–1009.
41 C. Y. Li, M. B. Luo, H. Li and W. P. Cao, *Colloid Polym. Sci.*, 2017, **295**, 2251–2260.
42 W. S. Tung, R. J. Composto, R. A. Riggleman and K. I. Winey, *Macromolecules*, 2015, **48**, 2324–2332.
43 T. Zhang, K. I. Winey and R. A. Riggleman, *Macromolecules*, 2019, **52**, 217–226.
44 K. Kremer and G. S. Grest, *J. Chem. Phys.*, 1990, **92**, 5057–5086.
45 R. Auhl, R. Everaers, G. S. Grest, K. Kremer and S. J. Plimpton, *J. Chem. Phys.*, 2003, **119**, 12718–12728.
46 G. S. Grest, M. D. Lacasse, K. Kremer and A. M. Gupta, *J. Chem. Phys.*, 1996, **105**, 10583–10594.
47 R. Kumar, M. Goswami, B. G. Sumpter, V. N. Novikov and A. P. Sokolov, *Phys. Chem. Chem. Phys.*, 2013, **15**, 4604–4609.
48 S. Plimpton, *J. Comput. Phys.*, 1995, **117**, 1–19.
49 Y. Jiang, J. L. Hor, D. Lee and K. T. Turner, *ACS Appl. Mater. Interfaces*, 2018, **10**, 44011–44017.
50 J. Han and H. G. Craighead, *J. Vac. Sci. Technol., A*, 1999, **17**, 2142–2147.
51 A. Squires and A. Meller, *Biophys. J.*, 2013, **105**, 543–544.
52 G. F. Schneider, S. W. Kowalczyk, V. E. Calado, G. Pandraud, H. W. Zandbergen, L. M. K. Vandersypen and C. Dekker, *Nano Lett.*, 2010, **10**, 3163–3167.
53 M. Möddel, W. Janke and M. Bachmann, *Phys. Chem. Chem. Phys.*, 2010, **12**, 11548–11554.
54 G. Giugliarelli and A. L. Stella, *J. Phys. A: Math. Gen.*, 1999, **32**, 5409–5418.